FINITE ELEMENT MODEL OF STRESS WAVE TOPOLOGY IN UNIDIRECTIONAL GRAPHITE/EPOXY: WAVE VELOCITIES AND FLUX DEVIATIONS*

R.D. Kriz and P.R. Heyliger**

Fracture and Deformation Division
National Institute of Standards and Technology
325 Broadway
Boulder, CO 80303

INTRODUCTION

Until recently, the use of a finite element model (FEM) to simulate stress wave propagation has been limited to solutions where the number of degrees of freedom are kept to a minimum, because of hardware limitations on computer memory and computational speed. With the advent of a number of new supercomputers, numerical simulation becomes a reasonable approach to some simpler problems. Recently, Ludwig, et. at [1,2] have demonstrated the feasibility of such an approach for problems where materials are either isotropic or only slightly anisotropic. We extend this effort to unidirectional graphite/epoxy which has large variations in elastic properties. For this material the effect of elastic anisotropy on stress wave propagation has been studied both experimentally and analytically [3,4] and several interesting properties have been predicted and measured: mode transitions, sensitivity of flux deviations to small changes in anisotropy, and shear wave speeds exceeding longitudinal waves. With a FEM we can simulate and study some of these properties most effectively.

FINITE ELEMENT MODEL

Governing Equations

For conditions of plane stress or plane strain the governing equations of motion in the two-dimensional domain Ω are

$$\frac{\partial \sigma_{xx}}{\partial x} + \frac{\partial \sigma_{xy}}{\partial y} = \rho \frac{\partial^2 u}{\partial t^2} \quad \text{and} \quad \frac{\partial \sigma_{xy}}{\partial x} + \frac{\partial \sigma_{yy}}{\partial y} = \rho \frac{\partial^2 v}{\partial t^2} , \tag{1}$$

---

*Contribution of the National Institute of Standards and Technology (formerly National Bureau of Standards), not subject to copyright.

**Current address: Civil Engineering Department, Colorado State University, Fort Collins, CO 80523

where $\sigma_{xx} = C_{11}\,\epsilon_{xx} + C_{12}\,\epsilon_{yy} + C_{16}\,\gamma_{xy}$

$$\sigma_{yy} = C_{12}\,\epsilon_{xx} + C_{22}\,\epsilon_{yy} + C_{26}\,\gamma_{xy} \qquad (2)$$

$\sigma_{xy} = C_{16}\,\epsilon_{xx} + C_{26}\,\epsilon_{yy} + C_{66}\,\gamma_{xy}$.

Here σ_{ij} are the stress components, u and v are displacements in the x and y coordinate directions respectively, ρ is the density, ϵ_{ij} and γ_{ij} are the strain components, C_{ij} represent the contracted stiffness for plane strain or the contracted-reduced stiffnesses for plane stress, and t is time.

We follow a standard semidiscrete variational formulation. First we substitute eqn. (2) into eqn. (1) and obtain the equations of motion written in terms of displacement u and v. We next multiply each of these equations by a sufficiently differentiable test function, taken as the first variation of the displacements components. Integrating these expressions by parts, using the Green-Gauss theorem, and substituting the following approximations for displacements,

$$u(x,y,t) = \sum_{j=1}^{n} u_j(t)\,\psi_j(x,y)$$

$$v(x,y,t) = \sum_{j=1}^{n} v_j(t)\,\psi_j(x,y) \qquad (3)$$

yields the equations of motion written in matrix form

$$\begin{bmatrix} [K^{11}] & [K^{12}] \\ [K^{21}] & [K^{22}] \end{bmatrix} \begin{Bmatrix} \{u\} \\ \{v\} \end{Bmatrix} + \begin{bmatrix} [M^{11}] & 0 \\ 0 & [M^{22}] \end{bmatrix} \begin{Bmatrix} \{\ddot{u}\} \\ \{\ddot{v}\} \end{Bmatrix} = \begin{Bmatrix} \{f^1\} \\ \{f^2\} \end{Bmatrix} . \qquad (4)$$

In eqns. (3) and (4) n is the number of nodes per element, subscripts denote nodal values, ψ_j is the j-th shape function of the element, and $\ddot{u}$ and $\ddot{v}$ are accelerations. The submatrices are:

$$K^{11}_{ij} = \int_\Omega \left[C_{11} \frac{\partial\psi_i}{\partial x}\frac{\partial\psi_j}{\partial x} + C_{16}\left(\frac{\partial\psi_i}{\partial x}\frac{\partial\psi_j}{\partial y} + \frac{\partial\psi_i}{\partial y}\frac{\partial\psi_j}{\partial y} \right) + C_{66} \frac{\partial\psi_i}{\partial y}\frac{\partial\psi_j}{\partial y} \right] dxdy , \qquad (5)$$

$$K^{21}_{ji}\ K^{12}_{ij} = \int_\Omega \left[C_{12} \frac{\partial\psi_i}{\partial x}\frac{\partial\psi_j}{\partial y} + C_{16} \frac{\partial\psi_i}{\partial x}\frac{\partial\psi_j}{\partial y} + C_{26} \frac{\partial\psi_i}{\partial y}\frac{\partial\psi_j}{\partial y} + C_{66} \frac{\partial\psi_i}{\partial y}\frac{\partial\psi_j}{\partial x} \right] dxdy , \qquad (6)$$

$$K_{ij}^{22} = \int_{\Omega}\left[C_{26}\left(\frac{\partial\psi_i}{\partial x}\frac{\partial\psi_j}{\partial y}+\frac{\partial\psi_i}{\partial y}\frac{\partial\psi_j}{\partial x}\right)+C_{66}\frac{\partial\psi_i}{\partial x}\frac{\partial\psi_j}{\partial x}+C_{22}\frac{\partial\psi_i}{\partial y}\frac{\partial\psi_j}{\partial y}\right]dxdy\ , \tag{7}$$

$$M_{ij}^{11} = \int_{\Omega}\rho\ \psi_i\psi_j dxdy = M_{ij}^{22}\ ,\ \text{and} \tag{8}$$

$$F_i^1 = \int_{\Gamma}\psi_i\hat{t}_x ds,\ F_i^2 = \int_{\Gamma}\psi_i\hat{t}_y ds\ . \tag{9}$$

where Ω is now the domain of a typical finite element, Γ is the boundary of Ω, and the prescribed displacements and tractions on the element boundary are defined below as the essential and natural boundary conditions.

$$\begin{matrix} u\ (x,y,t) = \hat{u} \\ \text{on } \Gamma \quad \text{and} \\ v\ (x,y,t) = \hat{v} \end{matrix} \qquad \begin{matrix} \sigma_{xx}n_x + \sigma_{xy}n_y = \hat{t}_x \\ \\ \sigma_{xy}n_x + \sigma_{yy}n_y = \hat{t}_y x \end{matrix} \tag{10}$$

The initial conditions are:

$$u\ (x,y,o) = \hat{u}_o \quad \text{and} \quad v(x,y,o) = \hat{v}_o\ . \tag{11}$$

Solution and Mesh Definition

The assembly, imposition of boundary conditions, and solution of eqn. (4) proceed as in standard finite element analysis [5]. The temporal solution of eqn. (4) is accomplished using the Newmark direct integration method as outlined in reference 5 where the constant-average-acceleration method required $\alpha = 1/4$, $\delta = 1/2$. Solutions were obtained by using an algorithm based on Gauss elimination.

A rectangular mesh, shown in Fig. 1, was constructed of 45 vertical and 180 horizontal elements for a total of 8100 elements and 8326 nodes. Each element is a four noded quadrilateral isoparametric element with a bilinear strain field. The global stiffness matrix had a total of 16458 degrees of freedom with a bandwidth of 96. The boundaries x=0 and x=L were constrained u=v=0. Memory requirements for the solution of eqn. (4) resulted in 3172857 single precision (64 bit) words on the NIST supercomputer. The solution for each time step took 2.25 minutes. The total solution time for a quasi-transverse (QT) wave (the slowest wave) to travel from y=0 to y=B was 2.2 hours. Small modifications in the equation solver were implemented so that parallel processing could be used to decrease solution time.

The dimension of each square element was scaled so that the quasi longitudinal (QL) wave (the fastest wave) would arrive at the surface y=B at the same time for different wave speeds. After a preliminary parametric study we chose a minimum of 9 elements per wavelength and 40 time increments per wave period. At the boundary y=0, sinusoidal displacements were prescribed at 10 consecutive nodes. The location of these nodes were chosen so that the QL and QT waves would reflect from the surface y=B without interfering with the constrained boundaries at x=o and x=L.

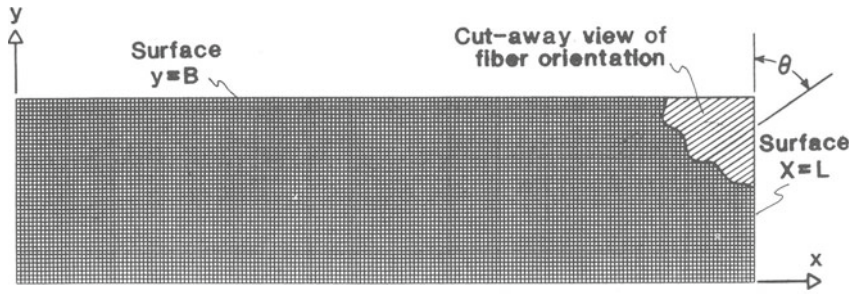

Fig. 1. Definition of finite element mesh.

Elastic Stiffness: Plane Stress and Plane Strain

Although we have confined our solution to a two-dimensional plane with conditions of plane stress or plane strain, the effect of the elastic anisotropy of the full elastic stiffness tensor $C_{ijk\ell}$ is nonetheless significant.

For unidirectional graphite/epoxy composites we confine our planar solutions to rotations, θ, of the fiber axis in a principle material plane, Fig. 1. Equations for predicting changes in stiffness, C_{ij}, with fiber orientation are given in [6]. Elastic stiffness (C_{11} = 161 GPa, $C_{22} = C_{33}$ = 14.5 GPa, $C_{12} = C_{13}$ = 6.5 GPa, C_{23} = 7.24 GPa, C_{44} = 3.63 GPa, $C_{55} = C_{66}$ = 7.1 GPa) are taken from [3]. It is not difficult to show that for plane strain ($\epsilon_3 = \epsilon_4 = \epsilon_5 = 0$) the compliances, S_{ij}, are reduced by the out-of-plane properties:

$$S'_{ij} = S_{ij} - S_{i3}S_{j3}/S_{33}^2 \ . \tag{12}$$

Similarly for plane stress ($\sigma_3 = \sigma_4 = \sigma_5 = 0$) the stiffnesses are also reduced by the out-of-plane properties:

$$C'_{ij} = C_{ij} - C_{i3}C_{j3}/C_{33}^2 \ . \tag{13}$$

It is interesting that $S_{ij} = [C'_{ij}]^{-1}$ and $C_{ij} = [S'_{ij}]^{-1}$ where the appropriate rows and columns have been eliminated. Tsai [7] discusses these interrelationships in some detail.

EXACT SOLUTION

Christoffel Solution

Stress-wave deformation fields in anisotropic media can be approximated by plane-wave solutions to the elastic-wave equation. This simplification leads to Christoffel equations [8]:

$$(C_{ijk\ell}\ \nu_j\ \nu_k - \rho v^2 \delta_{i\ell})\ p_\ell = 0 \ , \tag{14}$$

where $C_{ijk\ell}$ is the elastic-stiffness tensor, ν_j the wave vector, ρ the mass density, v the wave velocity (eigenvalue), $\delta_{i\ell}$ the Kronecker delta, and p_ℓ the direction of particle vibration (eigenvector). Solutions in the principal material planes are given in [9], where it is shown that the particle motion is confined to the principal material plane and

decouples from the out-of-plane vibrations. Hence the plane strain solutions and bulk wave solutions of eqn. (14) are identical when confined to principal material planes. For plane-stress, the solution of eqn. (14) is modified by reducing the stiffness by eqn. (13).

Flux Deviation

Musgrave [8] demonstrated graphically how the propagation direction can deviate from the wave vector. This direction is called the energy flux deviation vector,

$$E_j = C_{ijk\ell}\, u_{k,\ell}\, \dot{u}_i \ , \tag{15}$$

where u_i is the displacement vector for a plane wave. The velocity of propagation in the direction of E_j is called the group velocity. For anisotropic materials E_j deviates from ν_i by an angle, $\Delta=\cos^{-1}\nu_i E_i$.

The group velocity and deviation angle, Δ, is calculated differently for plane stress [10]:

$$\Delta = \tan^{-1} \Big[(\cos^2\theta C'_{11} + \sin^2\theta C'_{66} - \rho v^2)(2\cos\theta C'_{66}) + (\cos^2\theta C'_{66} + \sin^2\theta C'_{22} - \rho v^2)\,(2\cos\theta C'_{11}) - 2\cos\theta\sin^2\theta (C'_{12} + C'_{66})^2\Big] \Big/ \Big[(\cos^2\theta C'_{11} + \sin^2\theta C'_{66} - \rho v^2)\,(2\cos\theta C'_{22}) + (\cos^2\theta C'_{66} + \sin^2\theta C'_{22} - \rho v^2)\,(2\sin\theta C'_{66} - 2\cos^2\theta\sin^2\theta\,(C'_{12} + C'_{22})^2\Big]. \tag{16}$$

RESULTS AND DISCUSSION

The finite element solution of eqn. (4) for the region described in Fig. 1 was obtained for fiber orientations from $\theta=0^0$ to $\theta=90^0$ in increments of 10^0. Results are plotted as open symbols in Figs. 2a and 2b for conditions of plane strain and plane stress respectively. Results of eqns. (15) and (16) are plotted as lines in Figs. 2a and 2b for comparison. The comparison is excellent up to $\theta=70^0$. At larger angles the deviation between FEM results and eqns. (15) and (16) are very large and are not shown. The wave velocities predicted by FEM and eqn. (14) also compare well up to $\theta=60^0$ but are not shown here because of space limitations. These differences in velocities and flux deviations past $\theta=70^0$ are at present not accounted for.

Most interesting are the deformation fields (topology) of the stress waves traveling between surfaces y=0 and y=B. Here we show only topologies for the plane strain at $\theta=45^0$ and $\theta=70^0$ in Figs. 3 and 4. In Fig. 3 we can distinctly see two different types (QT and QL) but only the QL wave has reflected from the y=B boundary. Clearly the deformation field of the grid for the QL wave is mostly longitudinal with a smaller shear (transverse) component. The minimum principal stress shown in Fig. 4 can more clearly define the tunneling of the QT and QL waves but can not differentiate the wave types. Weak shear waves are more easily seen in Fig. 4. In Fig. 3 we see the reflected QL wave continues to propagate along the same path as predicted by theory [8].

The exact direction of propagation of both waves is difficult to measure in either Fig. 3 or Fig. 4. To solve this problem we extend

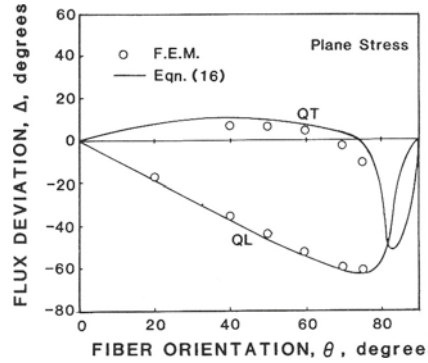

Fig. 2a. Comparison of FEM with theory for plane strain.

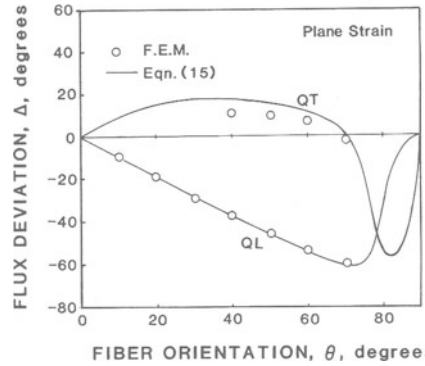

Fig. 2b. Comparison of FEM with theory for plane stress.

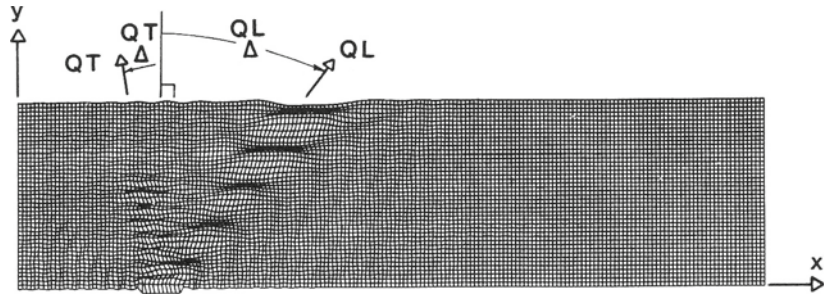

Fig. 3. Deformed grid showing QL and QT waves for plane strain with $\theta=45^0$.

solution times so that both waves reflected from the y=B boundary. We then plot the displacements along this boundary for one completed period. The family of curves defines an envelope from which the deviation angle can be measured: a line drawn through the center-line of the transducer and a line that connects the maximum amplitudes of the envelopes at the boundaries y=0 and y=B. From these envelope topologies we can also determine the degree of longitudinal and transverse components of each

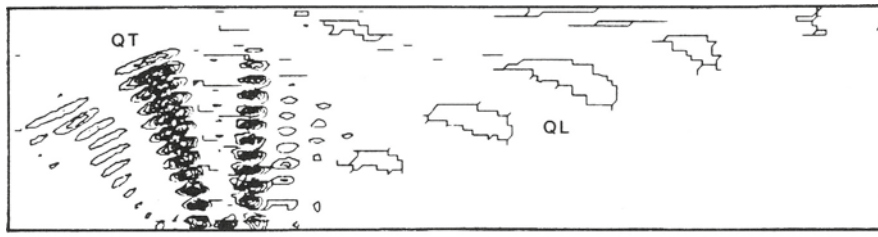

Fig. 4. Minimum principal stress plot of QL and QT waves for plane strain with $\theta=70^{o}$.

wave type. In Figs. 5a, 5b, we demonstrate a mode transition with increasing fiber-orientation: at $\theta=40^{o}$ the QL wave has the largest longitudinal component and this changes to a larger transverse component at $\theta=60^{o}$. Hence the QL wave is actually a QT wave and the QT wave has changed tc a QL wave at $\theta=60^{o}$. This same mode transition is predicted in [4] but with the FEM, this mode transition is seen more clearly.

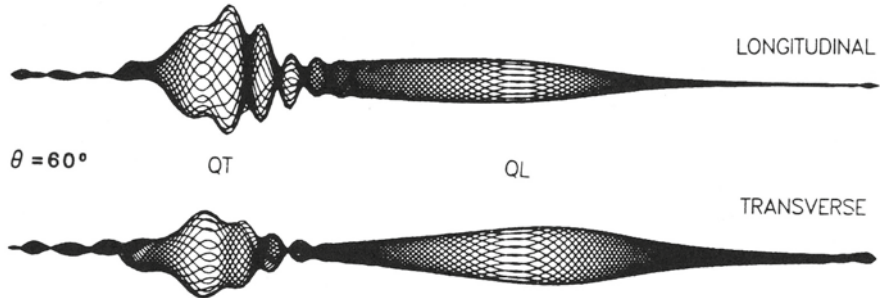

Fig. 5a. Deformations along y=B for one complete period with $\theta=40^{o}$.

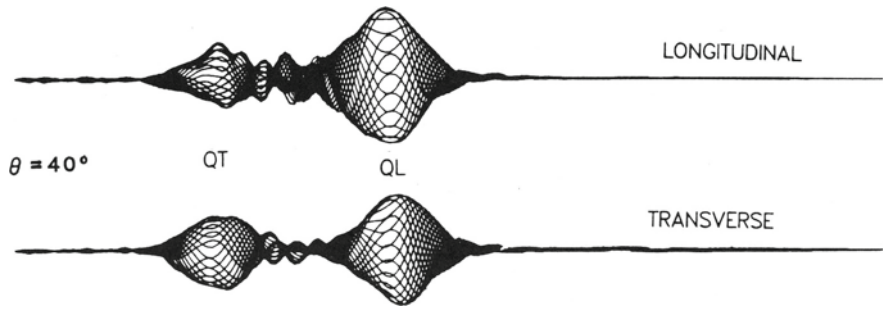

Fig. 5b. Deformations along y=B for one complete period with $\theta=60^{\circ}$.

CONCLUSIONS

With the FEM, topologies of stress wave deformation fields can accurately predict wave velocities, propagation directions, and wave types in highly anisotropic materials such as unidirectional graphite/epoxy. Previously predicted mode transitions have been confirmed by the FEM. Previously predicted tunneling and bifurcation of QL and QT were accurately simulated by the FEM in the range of $\theta=0^{\circ}$ to $\theta=70^{\circ}$ fiber orientations.

REFERENCES

1. R. Ludwig and W. Lord, Materials Evaluation 46, 108 (1988).

2. Z. You, W. Lord, and R. Ludwig, in Review of Progress in Quantitative NDE, edited by D.O. Thompson and D.E. Chimenti (Plenum Press, New York, 1988), Vol. 7A, pp. 23-30.

3. R.D. Kriz and W.W. Stinchcomb, Exper. Mech. 19, 41 (1979).

4. R.D. Kriz and H.M. Ledbetter, in Rheology in Anisotropic Materials, edited by C. Huet, D.Bourgoin and S. Richemond (CEPADUES-Editions, Toulouse, France, 1986) pp. 79-91.

5. K. Bathe and E.L. Wilson, Numerical Methods in Finite Element Analysis (Prentice-Hall, Englewood Cliffs, New Jersey, 1976).

6. R.M. Jones, Mechanics of Composite Materials (McGraw-Hill, New York, 1975).

7. S.W. Tsai, Composites Design - 1986 (Think Composites, Dayton, Ohio, 1986).

8. M.J.P. Musgrave, Crystal Acoustics (Holden-Day, San Francisco, 1970).

9. R.D. Kriz and H.M. Ledbetter, in Recent Advances in Composites in the United States and Japan, edited by J.R. Vinson and M. Taya (American Society for Testing and Materials, Philadelphia, 1985), pp. 661-675.

10. J.V. Foltz, A.L. Bertram, and C.W. Anderson, Report No. NSWC TR85-186, Naval Surface Weapons Center, Silver Spring, Maryland, June, 1985.